

## Chapter 2

# Hydrogen Trapping and Its Detection

### 2.1 Manifestations and Analyses of Hydrogen Trapping

#### 2.1.1 Solid Solubility at Low Temperatures

Hydrogen contents in steels are often of the order of 1 mass ppm. The values far exceed the solid solubility of hydrogen in iron at room temperature under ordinary environments and mostly result from trapping in various lattice defects. Figure 2.1 [1] is the extension of Fig. 1.2 for iron to lower temperatures. Data in the temperature range  $1/T > 20 \times 10^{-4}$  substantially scatter, and the specimens are mostly given cold-straining and successive annealing that produce various types of lattice defects.

Direct measurements of the solubility are difficult for very low concentrations of hydrogen at low temperatures. Hydrogen diffusivity is a measure of trapped states in lattice defects and is utilized for the estimation of hydrogen concentration even in case where weak hydrogen trapping exists. Permeation techniques are often employed for this purpose and the following is a brief description of the procedure.

The steady-state flow of hydrogen,  $J_{\infty}$ , in metal is described by Fick's first law of diffusion:

$$J_{\infty} = -D_H \frac{dC}{dx}, \quad (2.1)$$

where  $D_H$  is the diffusion coefficient of hydrogen and  $C$  is the hydrogen concentration. Assuming Sieverts' law for hydrogen concentrations at the input and output surfaces of the specimen, the total flux  $j_t$  of hydrogen permeating through a disk of area  $A$  and thickness  $L$  is expressed in terms of the permeability coefficient  $\Phi$  as

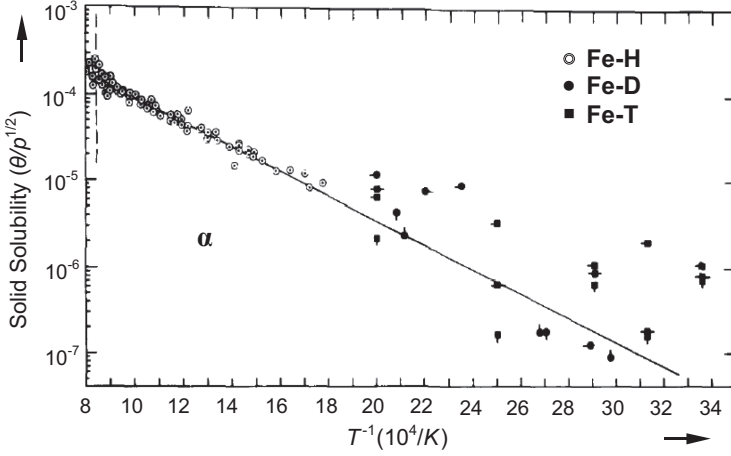


**Fig. 2.1** Solid solubility of hydrogen in iron in the temperature range from 20 °C to 900 °C (da Silva et al. [1])

$$j_t = \Phi \frac{A}{L} (p_i^{1/2} - p_o^{1/2}), \quad (2.2)$$

where  $p_i$  and  $p_o$  are pressures in the input and output surfaces, respectively. The numerical value of  $\Phi$  obtained for  $\alpha$ -iron above 100 °C is [2]

$$\Phi = (2.9 \pm 0.5) \times 10^{-3} \exp [(-35 \pm 1.8 \text{ kJ/mol})/RT], \quad (2.3)$$

where the units of  $\Phi$  is  $[\text{cm}^3(\text{ntp H}_2) \cdot \text{cm}^{-1} \cdot \text{s}^{-1} \cdot \text{atm}^{-1/2}]$ .

Electrochemical techniques are also used for hydrogen permeation from the gas phase through sheet specimens [3]. The permeability coefficient for pure iron thus obtained in temperature and pressure ranges of 0–60 °C and 0.01–1 atm, respectively, is

$$\Phi = 2.6 \times 10^{17} \exp [(-36 \pm 2.5 \text{ kJ/mol})/RT], \quad (2.4)$$

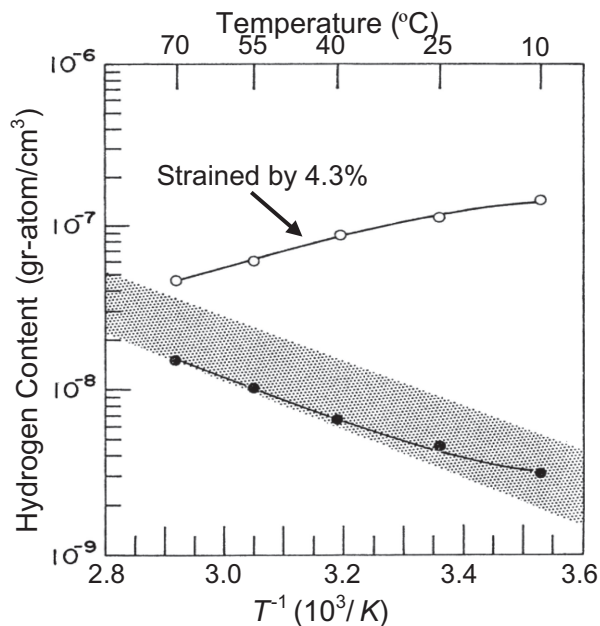
where the unit of  $\Phi$  is  $[\text{atom-H} \cdot \text{cm}^{-1} \cdot \text{s}^{-1} \cdot \text{atm}^{-1/2}]$ .

When the hydrogen pressure at the output surface is negligible, the hydrogen concentration at the input surface  $C_i$  in equilibrium with hydrogen gas of pressure  $p_i$  is obtained from Eqs. (2.1) and (2.2) using observed  $\Phi$  and  $D_H$  as

$$C_i = \frac{\Phi \sqrt{p_i}}{D_H}. \quad (2.5)$$

Equation (2.1) is also applied to the hydrogen entry by cathodic polarization, where  $C_i$  [ $\text{atoms-H} \cdot \text{cm}^{-3}$ ] is calculated from the steady-state current  $J_\infty$  [ $\text{atoms-H} \cdot \text{cm}^{-2} \cdot \text{s}^{-1}$ ] as

**Fig. 2.2** Temperature dependence of hydrogen content in iron with (○) and without (●) plastic strain of 4.3 % (Yamakawa et al. [4]. Reprinted with permission from The Japan Society of Corrosion Engineering)



$$C_i = \frac{J_{\infty} L}{D_H}. \quad (2.6)$$

Figure 2.2 [4] shows the result of an electrochemical permeation experiment with  $\alpha$ -iron single crystal specimens with/without prestraining. Tensile prestrain of 4.3 % was given at liquid nitrogen temperature, and the hydrogen concentration was calculated from the steady-state hydrogen flux. The temperature dependence of  $C_i$  for specimens without prestrain is consistent with the lower limit of the solubility data in Fig. 2.1 and shows the endothermic nature of the solid solution. On the contrary, the prestrain increases the hydrogen content to a large extent and also changes the hydrogen solutioning from endothermic to exothermic.

It is to be noticed that hydrogen composing  $C_i$  in Eqs. (2.5) and (2.6) is a quantity calculated from the boundary condition of the diffusion equation. The concentration of “diffusive” hydrogen includes not only hydrogen in solution but also weakly trapped hydrogen reversible to the solid solution to keep local equilibrium. The driving force of diffusion is the concentration gradient of lattice hydrogen, but the loss of lattice hydrogen by diffusion is compensated locally by reversibly trapped hydrogen.

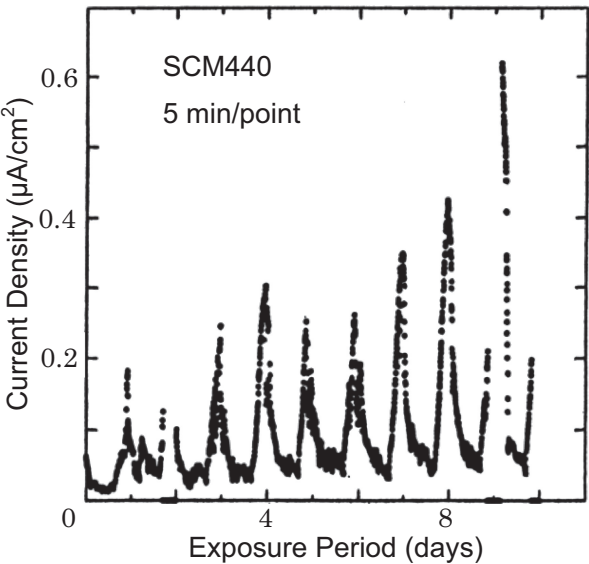
In electrochemical permeation experiments, the entry of hydrogen is controlled by the electrolyte and the applied cathodic polarization potential. The condition for electrolysis is crucial not only for the concentration of hydrogen in solution but also for trapped states of hydrogen. In this respect, the effective hydrogen fugacity in electrochemical experiments is an important quantity. Table 2.1 lists some reported

**Table 2.1** Effective hydrogen fugacity on the surface of electrode at cathodic electrolysis

Materials	Electrolyte	Current density (mA/cm <sup>2</sup> )	Hydrogen fugacity (atm)	Hydrogen pressure (atm)
99.5 iron	25 °C, distilled water	—	$5.7 \times 10^{-5}$	$5.7 \times 10^{-5}$
Armco iron	25 °C, 0.1 N NaOH	8.1	$2.2 \times 10^1$	$2.2 \times 10^1$
99.8 iron	25 °C, 0.1 N H <sub>2</sub> SO <sub>4</sub>	0.4	$5.4 \times 10^2$	$4.5 \times 10^2$
99.9965 iron	24 °C, 1 N H <sub>2</sub> SO <sub>4</sub> + 5 g/L As <sub>2</sub> O <sub>3</sub>	4.5	$1.2 \times 10^8$	$1.8 \times 10^4$
99.8 iron	25 °C, 0.1 N NaOH	1.8	$1.1 \times 10^0$	$1.1 \times 10^0$
99.8 Ferrovac E	25 °C, 0.1 N NaOH	11.3	$2.9 \times 10^1$	$2.9 \times 10^1$
AISI 1045	0.1 N H <sub>2</sub> SO <sub>4</sub> + 0.5 mg/L As <sub>2</sub> O <sub>3</sub>	0.4	$>1.4 \times 10^4$	
AISI 1045	0.1 N NaOH + 10 mg/L As <sub>2</sub> O <sub>3</sub>	0–0.6	$0 - 3 \times 10^3$	

Kumnick et al. [3] and Oriani et al. [5]

**Fig. 2.3** Alternating variation of the permeation current density through iron specimen exposed to natural atmospheric environment (Yamakawa et al. [6]. Reprinted with permission from The Iron & Steel Inst. Japan)



values pf hydrogen fugacity for iron and AISI 1045 steel estimated using Eq. (2.2) and permeability coefficients [3, 5].

Under corrosive atmospheric environments, the hydrogen entry into materials is controlled by electrochemical reactions on the surface, and the equivalent hydrogen fugacity varies with ambient atmospheres. Figure 2.3 [6] shows records of hydrogen permeation currents for a high strength Cr-Mo steel foil specimen, outer side of

which is exposed to atmospheric environment. The variation of the permeation current corresponds to daily alternations of humidity.

Permeation experiments are used for the measurement of the hydrogen diffusion coefficient that manifests hydrogen trapping. Details of the procedures and thus obtained information are described in Sect. 4.1.

### ***2.1.2 Hydrogen Thermal Desorption Analysis***

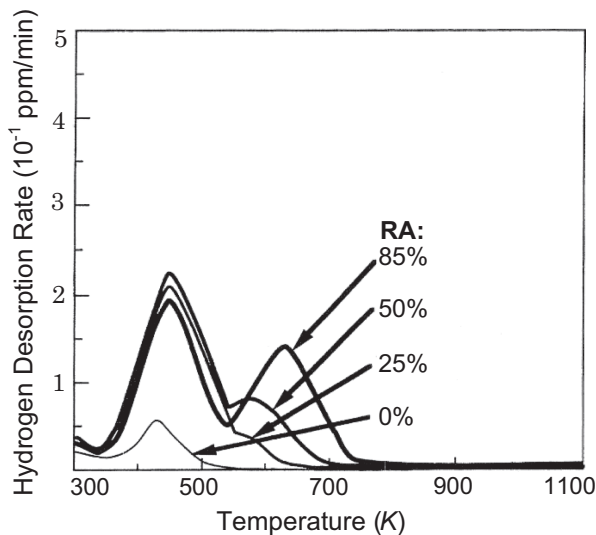
Analyses of the desorption of adsorbed gases from the metal surface under a controlled temperature ramp provide information on various parameters such as the number and populations of adsorbing phases, and the activation energy of desorption [7]. The thermal desorption spectroscopy (TDS) developed for characterizing adsorbed gases on the surface of material has been applied to hydrogen diffusing out from bulk specimens of metals [8–10]. The desorption-rate profile against temperature is affected by not only hydrogen states in the metal but also experimental parameters such the specimen size and the temperature-ramp rate. Accordingly, the terminology thermal desorption analysis (TDA) is more appropriate than TDS for the analysis of hydrogen states in metals.

In TDA, the measured quantity is the desorption rate of lattice hydrogen that diffuses out through the material undergoing trapping and detrapping processes. The rate-determining process of desorption during the temperature ramp differs by trapped states of hydrogen. When trapping is weak and local equilibrium exists between lattice and trapped hydrogen, thermally activated diffusion through lattice is the rate-determining process with a diffusion coefficient that depends on the density of and the binding energy with trap sites. On the other hand, when trapping is fairly strong, the thermally activated dissociation of trapped hydrogen with elevating temperature is the rate-determining process of desorption. Normally, desorption of strongly trapped hydrogen takes place at high temperatures, but the distinction between the two extreme processes is not simple and careful examinations of TDA are necessary.

Figure 2.4 [11] shows TDA profiles of hydrogen introduced to eutectoid steels cold-drawn to various reductions of area. Hydrogen was introduced by immersing the steel wires of 5 mm in diameter in a 20 %  $\text{NH}_4\text{SCN}$  aqueous solution at 323 K for 24 h, and the heating rate of TDA was 200 K/h. The specimen without cold-drawing shows a single desorption-rate peak with the peak temperature located at about 420 K. The amount of desorbed hydrogen increased with increasing reductions on cold-drawing, and an additional desorption peak appeared at higher temperatures. The increase initially appeared in TDA profiles for the lower temperature peak and successively for the higher temperature one.

Hydrogen states corresponding to the two peaks are quite different. For TDA of the specimen cold-drawn by 85 %, the lower temperature peak almost totally disappeared after exposing the specimen at room temperature for 2 weeks, indicating that hydrogen composing the lower temperature peak is diffusive. On the

**Fig. 2.4** Thermal desorption curves of hydrogen introduced to eutectoid steel specimens cold-drawn to various reductions of area (Takai et al. [11])



contrary, the higher temperature peak was hardly affected by room temperature exposure, indicating non-diffusive nature of trapped hydrogen.

For pure iron, the hydrogen absorption capacity increases by cold-drawing, but only a single desorption peak appears at about 400~500 K on TDA profiles depending on the specimens size [11]. The peak disappears when hydrogen-charged specimens are exposed at room temperature, indicating diffusive nature of hydrogen. Lattice defects that concern with the single peak in TDA profile is described in Chap. 3. On the other hand, the trap sites of non-diffusive hydrogen that composes the higher temperature peak in Fig. 2.4 for cold-drawn eutectoid steels must be created by heavy deformation of eutectoid cementite, but the entity of trapping is not definite.

#### (a) Dissociation-controlled desorption

The quantities that describe hydrogen trapping are density of trap site, hydrogen occupancy therein and binding energy of hydrogen therewith. Some procedures have been devised to estimate these quantities from TDA. Kissinger expressed the reaction rate of thermal dissociation of minerals, e.g., solid  $\rightarrow$  solid + gas, in the form [12]

$$\frac{dX}{dt} = A(1 - X)^n \exp\left(-\frac{E_a}{RT}\right), \quad (2.7)$$

where  $X$  is the fraction reacted,  $A$  is the reaction constant,  $n$  is the order of the reaction and  $E_a$  is the activation energy of the reaction. This type of equation was applied to the thermal desorption of gases from metal surfaces [7] and also to the thermal detrapping of hydrogen from trap sites in metals [8].

The peak temperature  $T_p$  at which the dissociation rate is maximum is obtained by differentiating Eq. (2.7) with  $t$ , i.e.,

$$\frac{d}{dt} \left( \frac{dX}{dt} \right) = \frac{dX}{dt} \left[ \frac{\varphi E_a}{RT^2} - A \exp \left( -\frac{E_a}{RT} \right) \right] = 0, \quad (2.8)$$

or

$$\frac{\varphi E_a}{RT_p^2} = A \exp \left( -\frac{E_a}{RT_p} \right), \quad (2.9)$$

for a reaction of the first order ( $n = 1$ ) and a linear heating rate,

$$T = T_0 + \varphi t. \quad (2.10)$$

Differentiation with  $1/T_p$  of the logarithm of Eq. (2.9) gives

$$\frac{\partial \ln \left( \varphi / T_p^2 \right)}{\partial (1/T_p)} = -\frac{E_a}{R}, \quad (2.11)$$

Then, the activation energy of detrapping,  $E_a$ , is obtained from the gradient of the plot of  $\ln (\varphi / T_p^2)$  vs.  $(1/T_p)$  using measured  $T_p$  at various heating rates.

It should be noticed that the above method of evaluating  $E_a$  is valid when the desorption is rate-limited by the dissociation of trapped hydrogen rather than by diffusion of hydrogen in lattice. The condition is satisfied for strongly trapped hydrogen, and a criterion for the applicability is the magnitude of the binding energy with traps. Suggested magnitudes of  $E_a$  at the border of reversible or irreversible traps are 26.4 kJ/mol for  $E_a$  [13] or 64 kJ/mol for  $E_b$  [14] for iron at room temperature. The experimentally determined  $E_a$  of the higher temperature peak in Fig. 2.2 according to Eq. (2.11) was 65 kJ/mol [15].

Turnbull et al. noticed from a more rigorous treatment [16] that the application of Kissinger's equation, Eq. (2.7), is valid for a very low trap occupancy in case of low lattice hydrogen contents as described in (c) of this section. An experimental method to check whether desorption is dissociation-controlled or not is the dependence of TDA profiles on the specimen size. For the dissociation-controlled desorption, TDA profiles are unaffected by the specimen size since  $A$  in Eq. (2.7) is a constant irrelevant to the specimen size.

#### (b) Diffusion-controlled desorption

On the other hand, when the desorption rate is limited by diffusion of hydrogen in metals, parameters of hydrogen trapping are estimated by modeling TDA profiles. Basic diffusion theories are described in Sect. 4.2, and some examples of the use of trapping parameters for modeling TDA profiles are presented here.

Trapping and detrapping sequences during the migration process of hydrogen are incorporated in the diffusion coefficient. Fick's diffusion law, Eq. (2.1), for the flow of lattice hydrogen is applied to the gradient of total hydrogen concentration  $C_T$  that includes trapped hydrogen in equilibrium with lattice hydrogen. The diffusion equation is expressed using the apparent or effective diffusion coefficient  $D_{\text{eff}}$  that depends on trapped states, i.e.,

$$J = -D_{\text{eff}} \frac{dC_T}{dx}. \quad (2.12)$$

Oriani expressed  $D_{\text{eff}}$  considering equilibrium between atomic populations in the normal lattice and traps [14]. When hydrogen occupies a fraction  $\theta$  of available sites, the equilibrium constant  $K$  is the ratio of the activity of hydrogen in the trap sites to that in lattice sites. For very low  $C_L$ , i.e.,  $\theta_L \ll 1$ ,  $K$  is expressed in terms of the fractional occupancy in the form of

$$K = \frac{1}{\theta_L} \left( \frac{\theta_x}{1 - \theta_x} \right), \quad (2.13)$$

where suffices  $x$  and  $L$  denote trapping and normal lattice sites, respectively. The local equilibrium that Oriani assumed was that a change of the lattice hydrogen concentration is compensated in the same time interval by the same amount of trapped hydrogen to keep equilibrium.

When the hydrogen concentration  $C$  is defined as the number of hydrogen atoms per unit volume,  $C$  is the product of the number of sites per unit volume,  $N$ , and the fractional occupancy,  $\theta$ , thereof. Then,

$$C_L = N_L \theta_L, \quad (2.14)$$

and

$$C_x = N_x \theta_x. \quad (2.15)$$

It is to be noticed that  $N$  includes the coordination number available for hydrogen around one lattice or defect site of host metals.

Comparing Eqs. (2.1) and (2.12) for Fick's first law,  $D_{\text{eff}}$  is related to the normal diffusivity  $D_L$  and trapping parameters in Eqs. (2.13) and (2.15) in the form of

$$D_{\text{eff}} = D_L \frac{dC_L}{dC_T} = D_L \left[ 1 + \frac{N_x N_L K}{(N_L + K C_L)^2} \right]^{-1} \quad (2.16)$$

or

$$D_{\text{eff}} = D_L \frac{C_L}{C_L + C_x(1 - \theta_x)} \quad (2.17)$$

For  $\theta_x \ll 1$ , i.e., for a very low occupancy of trapping sites,



$$D_{\text{eff}} = D_L \frac{C_L}{C_T}. \quad (2.18)$$

When  $C_L$  is very small, Eq. (2.16) is written in terms of the density of trap sites,  $\Gamma_x$  ( $= N_x/N_L$ ), and the binding energy  $E_b$  as

$$D_{\text{eff}} = D_L \left[ 1 + \Gamma_x \exp \left( \frac{E_b}{RT} \right) \right]^{-1}. \quad (2.19)$$

Ono and Meshii considered dynamic equilibrium between trapping and detrapping processes and obtained an expression of  $D_{\text{eff}}$  similar to Eq. (2.19), multiplying the exponential factor therein by entropy factor [10].

The desorption rate is calculated from the solution of Fick's second law of diffusion,

$$\frac{\partial C}{\partial t} = D \frac{\partial^2 C}{\partial x^2}, \quad (2.20)$$

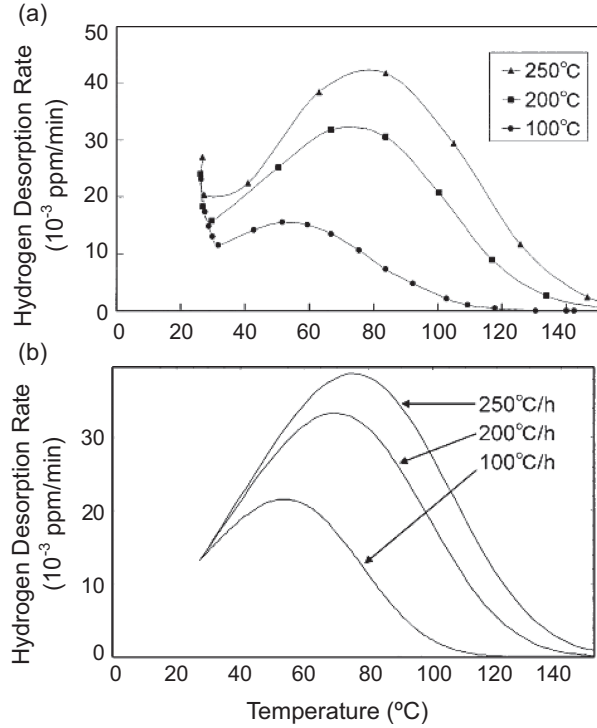
with proper initial and boundary conditions. Ono and Meshii simulated TDA profiles of quenched-in hydrogen from high temperatures in pure iron specimens. Observed TDA profiles showed a single desorption peak at about 420 K, excluding an artifact peak at 220 K due to desorption of water molecules from the metal surface. Computations by means of a finite difference method gave simulated TDA profiles coincident with observed ones using  $D_{\text{eff}}$  with  $E_b = 51$  kJ/mol and  $\Gamma_x = (4 \sim 15) \times 10^{-5}$  in Eq. (2.19).

Effects of trapping parameters in TDA profiles were examined by Yamaguchi and Nagumo using effective diffusion coefficients [17]. The specimens were martensitic steel plates and experimental variables were the plate thickness, the amount of prestrain to vary the density of defects, the hydrogen-charging time to vary the initial distribution of hydrogen in specimen and the heating rate. Hydrogen as a tracer of lattice defects was introduced to deformed specimen by fairly mild cathodic electrolysis using a 3 % NaCl + 3 g/l  $\text{NH}_4\text{SCN}$  aqueous solution at a current density of 5 A/m<sup>2</sup>. The mild condition prevented to induce extraneous defects. Simulations of TDA profiles were conducted using Eq. (2.20) with  $D_{\text{eff}}$  defined by Eq. (2.19) that includes  $\Gamma_x$  and  $E_b$  as fitting parameters.

Figure 2.5 [17] compares observed and simulated TDA profiles for specimens of 2 mm in thickness with increasing heating rates. For the calculation,  $\Gamma_x$  and  $E_b$  were assumed to be  $8.5 \times 10^{-2}$  and 17 kJ/mol, respectively. Figure 2.6 [17] also compares observed and simulated TDA profiles for specimens given different amounts of strain. For the calculation,  $E_b$  was fixed at 20 kJ/mol and  $\Gamma_x$  was varied.

The peak temperature  $T_p$  at which the desorption rate is maximum shifts to higher temperatures with increasing  $E_b$ , as shown in Fig. 2.7(a) [17], but  $T_p$  is also a function of  $\Gamma_x$  as shown in Fig. 2.7(b) [17]. Accordingly, a unique combination of  $\Gamma_x$  and  $E_b$  is not determined by modeling an observed  $T_p$ . Another measure of fitting

**Fig. 2.5** Thermal desorption curves of hydrogen from martensitic steel specimens of 2 mm in thickness at various heating rates. **(a)** Experimental curves, **(b)** simulation curves (Yamaguchi et al. [17])



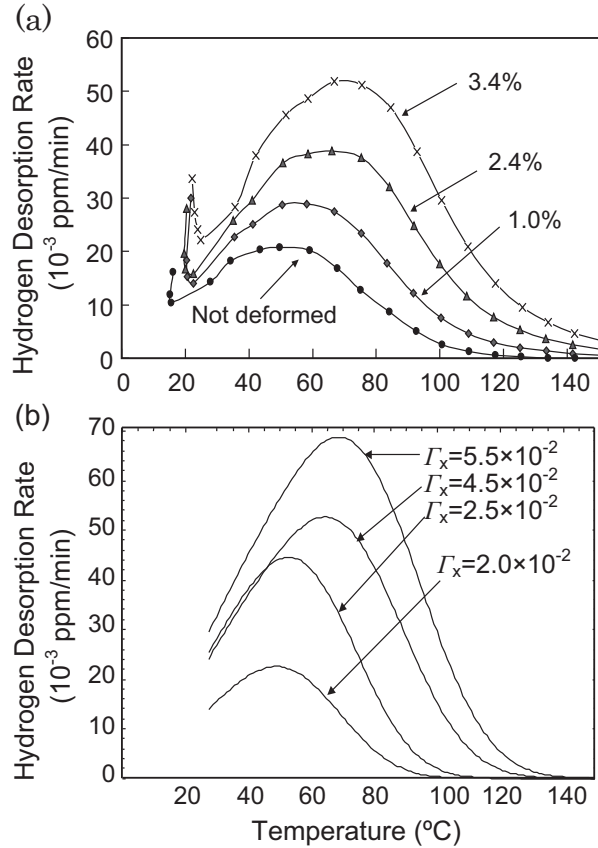
is the desorption-rate peak width. The peak width at the same  $T_p$  is broader when calculated using larger  $\Gamma_x$  and smaller  $E_b$  values. A proper characterization of TDA profile in addition to  $T_p$  is necessary in utilizing modeling to estimate trapping parameters. It is also to be noticed that TDA profiles depend on geometries of specimen in case of the diffusion-controlled desorption.

TDA gives useful information on lattice defects that affect hydrogen-related failure, but one should be aware that an exact estimation of trapped states of hydrogen is not straightforward in the case of diffusion-controlled desorption.

#### (c) General treatments in case of multiple traps

Desorption peaks in TDA often exhibit asymmetry accompanying broadening of the width and hump(s) or sub-peak(s). Such features manifest the existence of multiple types of trap. A general formulation of diffusion accompanying trapping processes was given by McNabb and Foster [18] by adding a term for the interchange of hydrogen atoms between diffusing and trapped states in Fick's second law. The equation is

**Fig. 2.6** Thermal desorption curves of hydrogen from martensitic steel specimens of 2 mm in thickness given various amounts of strain. (a) Experimental curves, (b) simulation curves for traps of the binding energy of 20 kJ/mol and different densities  $\Gamma_x$ . The heating rate is 100 °C/h (Yamaguchi et al. [17])



$$\frac{\partial C_L}{\partial t} + \sum_i N_i \frac{\partial \theta_i}{\partial t} = D_L \tilde{N}^2 C_L, \quad (2.21)$$

with

$$\frac{\partial \theta_i}{\partial t} = k_i C_L (1 - \theta_i) - p_i \theta_i, \quad (2.22)$$

where  $N$ ,  $C_L$  and  $\theta$  are defined in Eqs. (2.14) and (2.15) and  $k$  and  $p$  are respectively trapping- and detrapping-rate parameters. The terms  $k_i C_L (1 - \theta_i) N_i$  and  $p_i \theta_i N_i$  are respectively the number of hydrogen atoms captured at and released from the  $i$ -th trap in unit volume per second.

Trapping and detrapping are thermally activated processes, and  $k$  and  $p$  are related to potential energies denoted in Fig. 2.8. Expressions of  $k$  and  $p$  are given as [16]

**Fig. 2.7** Effects of (a) the binding energy with hydrogen and (b) the density of the trap on simulated thermal desorption curves. (a) The trap density is fixed at  $1.0 \times 10^{-4}$ ; (b) the binding energy is fixed at 58.6 kJ/mol. The plate thickness is 2 mm and the heating rate is 100 °C/h (Yamaguchi et al. [17])

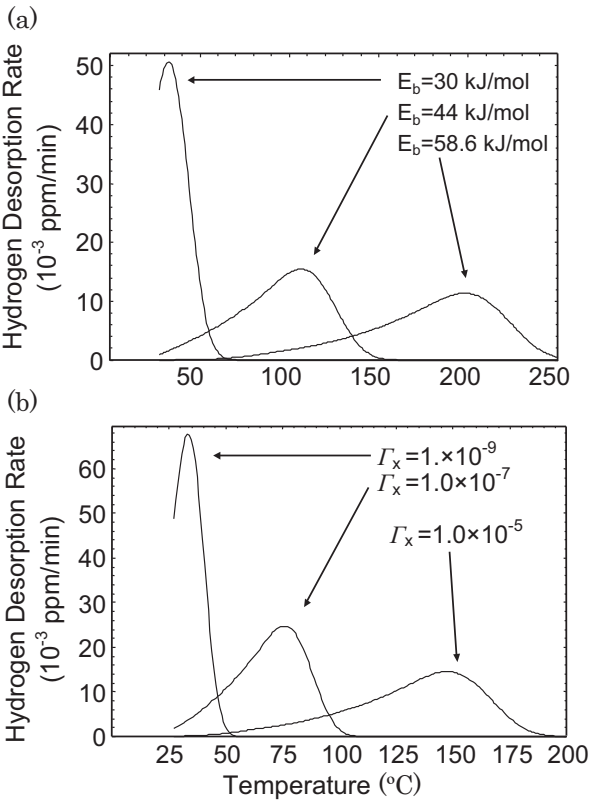
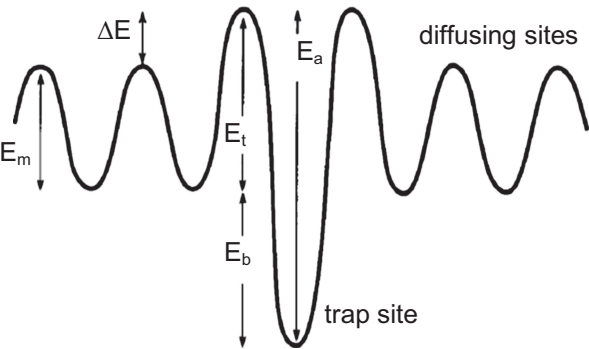


**Fig. 2.8** Schematic illustration of energy states of lattice and trapped hydrogen in metals



$$\begin{aligned} k &= k_0 \exp \left( -\frac{E_t}{RT} \right), \\ p &= p_0 \exp \left( -\frac{E_b + E_t}{RT} \right). \end{aligned} \quad (2.23)$$

In Fig. 2.8, the change in the saddle point energy  $\Delta E$  is either positive or negative according to the relative magnitude of  $E_t$  and  $E_m$ . Parameters  $p$  and  $k$  are not independent. When the occupation of hydrogen in the trap is low enough, the ratio  $k/p$  in the steady-state condition ( $\partial\theta/\partial t = 0$ ) gives

$$\frac{k_0}{p_0} = \frac{1}{N_L(1-\theta)} \approx \frac{1}{N_L} = \text{constant}. \quad (2.24)$$

The general solution of Eqs. (2.21) and (2.12) is difficult. McNabb and Foster derived an approximate solution for thick specimens, i.e., for the case where frequent trapping and detrapping take place during the time of diffusion, under dynamic equilibrium between trapped and lattice hydrogen [18]. When the hydrogen concentration is low enough, Eq. (2.21) is reduced to Fick's first law by using  $D_{\text{eff}}$  defined as

$$D_{\text{eff}} = D_L \left( 1 + N_x \frac{k}{p} \right)^{-1}. \quad (2.25)$$

Equation (2.25) is a kinematic expression of Oriani's  $D_{\text{eff}}$ , Eq. (2.19), which is derived from the local equilibrium concept. Further descriptions on hydrogen diffusion process are in Sect. 4.2 about permeation experiments.

TDA profiles are affected by trapping parameters as described in Sect. 2.1.2(b). Turnbull et al. simulated TDA profiles by solving Eqs. (2.21) and (2.22) using a finite differential method [16]. In the analysis, the ratio  $k/p$  is important and the functional form of  $D_{\text{eff}}$  in Eq. (2.25) is similar to that in Eq. (2.19). Then, calculated TDA profiles obtained using Eqs. (2.19) and (2.25) are similar. For the case of a single trap, key material variables that determine TDA profile are the density of trap sites and the binding energy. Their effects are similar to those shown in Figs. 2.5 and 2.6 obtained by using the effective diffusivity. The peak hydrogen flux and the peak temperature have no marked dependence on the magnitude of rate constants  $k_0$  and  $p_0$  [16]. Impacts of test parameters such as the heating rate and the sample thickness are also similar between the two modeling methods [16, 17]. The increase in  $C_0$  enhances the desorption in the lower temperature side of the peak and shifts the desorption peak to lower temperature [17]. An explanation is that the higher  $C_0$  causes the higher occupancy of traps and reduces retrapping of diffusing lattice hydrogen, resulting in the faster diffusion at lower temperatures.

Turnbull et al. extended their calculations to the case of two types of traps [16], i.e.,  $i = 1$  and  $2$  in Eq. (2.21). The calculated TDA profile for two traps with binding energies of 48 and 68 kJ/mol, respectively, exhibits two discrete peaks. Each peak is

the same as the one expected for the case of a single trap of 48 or 68 kJ/mol in the binding energy. However, when binding energies are closer, *e.g.*, 48 and 58 kJ/mol, the two peaks merge into one peak. In the calculation, the densities of the two traps are assumed to be the same. The appearance of discrete peaks should depend not only on the difference of the binding energies but also on their magnitudes and on the densities of traps.

Modeling of TDA profiles using McNabb-Foster's equation were attempted by Enomoto et al. using a finite difference method [19]. The observed TDA profile of hydrogen from martensitic steel showed a single peak, and Enomoto et al. assumed trapping of hydrogen in the elastic strain field of dislocations. The binding energy of 27 kJ/mol and the density of trap sites were assumed from the literature, and the fractional occupancy was estimated from the observed amount of hydrogen. Trapping and detrapping parameters in Eq. (2.23) were determined so as to match the calculated peak temperature and desorption rate to observed ones. Thus, determined ratio  $p_0/k_0$  of the order of  $10^{29}/\text{m}^3$  is nearly coincident with the values employed by Turnbull et al. [16].

Enomoto et al. also simulated TDA profiles that exhibited two desorption-rate peaks as shown in Fig. 2.4 for a cold-drawn eutectoid steel bar specimen [19]. They assumed that the two peaks were due to the elastic strain field and the core of dislocation with binding energies of 27 and 50 kJ/mol, respectively, from the literature. The trap densities and the initial fractional occupancies of the traps were estimated by assuming the dislocation density of  $10^{16} \text{ m}^{-2}$  and observed hydrogen fluxes of the two peaks. For the ratio  $p_0/k_0$ , the value formerly determined for martensitic steel was also used. A part of hydrogen introduced into specimen diffused out during room temperature exposure, and the simulation satisfactorily reproduced the observed decay of the lower temperature peak in TDA profiles. However, it should be noticed that a set of parameters is not unique to a given TDA profile. Their assignments of trap sites to microstructures are not reasonable, and many assumptions requisite for calculations must be carefully examined.

#### (d) Technical and intrinsic problems

TDA is a powerful tool for investigating trapped states of hydrogen in metals, but the analyses described above have some limitations for identifying trapped states of hydrogen. At conventional TDA procedures, a substantial amount of hydrogen is lost prior to the start of the temperature ramp. A new method, low temperature thermal desorption spectroscopy (LTDS), starts the temperature ramp from a temperature as low as 70 K [20]. The desorption takes place in low diffusivity range, and early parts of desorption is correctly measured without an inevitable loss of hydrogen that happens in conventional TDA. LTDS enables to obtain the complete form of TDA profile as shown in Fig. 2.9 [20] that compares conventional TDA and LTDS profiles of hydrogen introduced into a plastically deformed pure iron specimen of 0.5 mm in thickness. Examples of LTDS are also shown in Figs. 3.10 and 3.11 in Sect. 3.2.3(b).

Trapping parameters,  $k$  and  $p$  in Eq. (2.22), are used in the form of  $k/p$  for modeling. A method to separate the parameters was devised by Pound

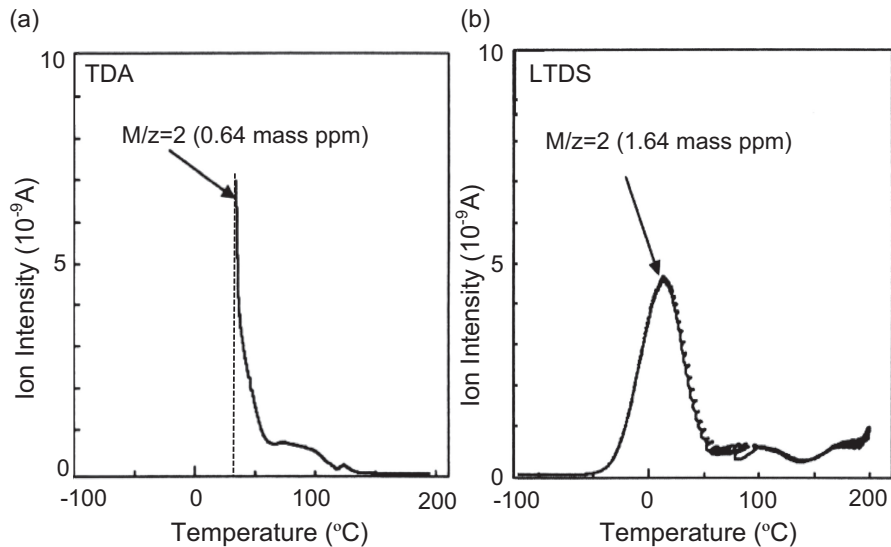


**Fig. 2.9** Comparison of TDA and LTDS curves of hydrogen from 90 % cold-rolled iron specimens of 0.5 mm in thickness. Hydrogen is charged by immersing the specimens in 20 %  $\text{NH}_4\text{SCN}$  aq at 50 °C for 24 h (Sato et al. [20], Reprinted with permission from The Iron & Steel Inst. Japan)

et al. [21]. On electrochemical permeation, a double-step method was devised to introduce hydrogen into the metal specimen, firstly at a cathodic potential for a short time and then stepping-up the potential to a more positive value to remove diffusive hydrogen. The amount of removed hydrogen was counted as the anodic charge from the transient anodic current, and the difference between the total charge passed into the metal and the charge passed out during the discharge gave the amount of irreversibly trapped hydrogen. It was assumed that the change of hydrogen concentration with time was due to the diffusional flow and the capture in irreversible traps. The trapping-rate parameter,  $\kappa$ , was defined as

$$\kappa = kN_x(1 - \theta_x), \quad (2.26)$$

including trapping parameters  $k$  and  $N_x$  defined in Eqs. (2.21) and (2.22). Experiments conducted for iron in aqueous  $\text{H}_2\text{S}$  solutions gave the values of  $\kappa$  of  $0.25 \text{ s}^{-1}$  that decreases to  $0.05 \text{ s}^{-1}$  by annealing, but the nature of the irreversible trap sites were not definite.

On TDA measurements, temperature ramping occasionally alters defect structures in materials. Microstructures of steels are not always thermally stable as envisaged on tempering of martensite or recovery of plastically strained materials. In such cases, thermal desorption of hydrogen takes place not only by the activated diffusion or thermal release from traps but also is associated with alterations of trapping defects themselves, such as precipitation of carbides, reconfiguration of

dislocations and annihilation of point defects. Analysis of TDA profile taking into account such structural alterations during temperature ramp has not been established.

The binding energy of hydrogen with traps is a major factor that determines the desorption rate. Local equilibrium that is a premise for the diffusion-controlled desorption is viable for  $E_b$  lower than a border value. However, the border value is a function of temperature [14], and the rate-controlling process for desorption occasionally changes during the temperature ramp. Such situations pose difficulties in selecting proper approximations for the analyses. In the case of diffusion-controlled desorption from multiple types of traps, separation of respective traps is difficult when hydrogen in each trap is in local equilibrium with lattice hydrogen. LTDS has been devised to improve the precision of analysis and also to separate desorption peaks arising from traps with close  $E_b$ s. Separation of weakly trapped states of hydrogen using LTDS is described in Sect. 3.2.3(b), but modeling of observed LTDS profiles is not yet conducted.

It is again to be noticed that trapping parameters estimated from a TDA profile, such as the binding energy and the trap density, do not straightly indicate microscopic entities of the trap. The parameters for a supposed type of defect are to be determined separately, and their consistency with modeling of TDA profiles is a proper procedure to identify hydrogen traps by means of TDA.

## 2.2 Partition of Hydrogen Among Different Traps

### 2.2.1 *Equilibrium Distribution*

The number of hydrogen atoms trapped in a type of defect is the product of the number of sites and the fractional occupancy by hydrogen. The distribution function for the partition of hydrogen among different sites was discussed by Hirth and Carnahan [22] with respect to the adsorption of hydrogen at dislocations and cracks in iron. From thermodynamics viewpoint, McLellan derived the distribution of hydrogen among trap sites and neighboring normal lattice sites in terms of the Fermi-Dirac distribution provided that the fractional occupancy was low and mutual interactions of trapped hydrogen atoms were negligible [23].

The Fermi-Dirac distribution expresses the probability  $f(E)$  that a particle will have energy  $E$  as

$$f(E) = \frac{1}{1 + \exp [(E - E_F)/k_B T]}, \quad (2.27)$$

where  $k_B$  is the Boltzmann constant and  $E_F$  is the Fermi energy. Then, the numbers of hydrogen atoms  $N_H$  in two energy states,  $E_0$  and  $E_1 = E_0 - E_b$ , are given as



$$\frac{N_{H0}}{N_0 - N_{H0}} \exp\left(-\frac{E_0}{k_B T}\right) = \frac{N_{H1}}{N_1 - N_{H1}} \exp\left(-\frac{E_1}{k_B T}\right). \quad (2.28)$$

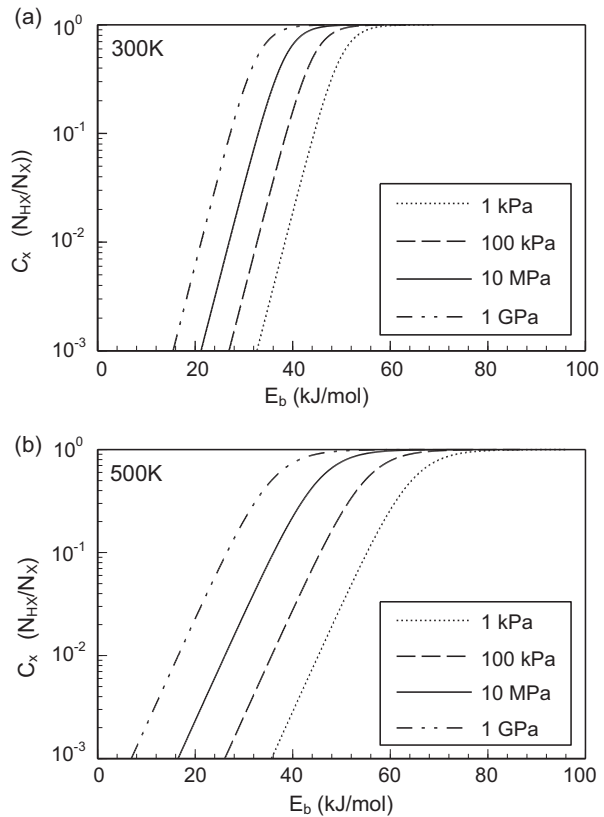
by changing the sign of a binding energy to be negative.  $N$  and  $N_H$  denote the number of a site and the number of hydrogen in the site, respectively [24]. Denoting the state 0 and 1 for the normal lattice and trapped state, respectively, Eq. (2.28) is written in terms of fractional occupancy,  $\theta$ , as

$$\begin{aligned} \frac{\theta_x}{1 - \theta_x} &= \frac{\theta_L}{1 - \theta_L} \exp\left(1 - \frac{E_L - E_x}{k_B T}\right) = \frac{\theta_L}{1 - \theta_L} \exp\left(\frac{E_b}{k_B T}\right) \\ &\approx \theta_L \exp\left(\frac{E_b}{k_B T}\right), \end{aligned} \quad (2.29)$$

showing an approximate Boltzmann distribution when  $\theta_x \ll 1$ .

The variation of  $\theta_x$  against  $E_b$  calculated from Eq. (2.29) is shown in Fig. 2.10 for iron under hydrogen gas environments at 300 and 500 K, using  $\theta_L$  calculated from Sieverts' law. Under a constant pressure,  $\ln \theta_x$  is proportional to  $E_b$  for low  $\theta_x$ , but

**Fig. 2.10** Calculated hydrogen occupation of traps in iron with various binding energies under hydrogen gas environments at (a) 300 K and (b) 500 K. Calculation is conducted using the Fermi-Dirac distribution and the occupation is denoted in terms of the atomic ratio at traps



the linear relationship no longer holds when  $\theta_x$  approaches saturation exceeding *ca.* 0.3 under high pressures. Accordingly, the ratio of the amounts of hydrogen trapped in sites of different  $E_b$  is not constant but varies by environments. From Eq. (2.29), the ratio of  $\theta_x$  of two trap sites with different  $E_b$  is

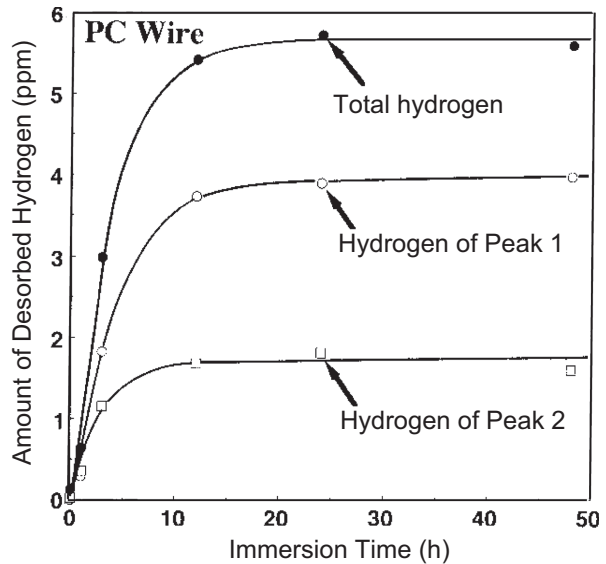
$$\frac{\theta_{x1}}{\theta_{x2}} = \frac{1 - \theta_{x1}}{1 - \theta_{x2}} \exp \left( \frac{E_{b1} - E_{b2}}{k_B T} \right). \quad (2.30)$$

The ratio is a function of  $\theta_L$  which varies with the fugacity of hydrogen. Under a constant fugacity,  $\theta_x$  at a site of a higher  $E_b$  is larger than that at sites of lower  $E_b$ . When fugacity increases and  $\theta_x$  at a site of a higher  $E_b$  approaches saturation, the ratio of  $\theta_x$ s tends to deviate from the linear relationship. In laboratory tests to assess the susceptibility to hydrogen embrittlement, introduced hydrogen distributes among various lattice defects that play different roles in embrittlement. The hydrogen occupancy is crucial for a specific type of defect to operate in the fracture process. Thus, a proper choice of hydrogen-charging conditions, such as electrolyte and current density in the case of cathodic electrolysis, is necessary for discriminating defects that contribute to hydrogen embrittlement.

### 2.2.2 Kinetics of Hydrogen Trapping

Fracture events most often proceed under nonequilibrium conditions. Trapping of hydrogen in various defects proceeds sequentially on the entry of hydrogen and

**Fig. 2.11** The amount of desorbed hydrogen from cold-drawn eutectoid steel wires subjected to the FIP test for increasing periods. The reduction of specimens at cold-drawing is 75 % (Takai et al. [25]. Reprinted with permission from The Iron & Steel Inst. Japan)



during loading. Figure 2.11 [25] shows the increase in the two peaks in TDA profiles of a eutectoid steel cold-drawn by 75 % and subjected to sustained loading in a 20 %  $\text{NH}_4\text{SCN}$  aqueous solution at 323 K. The TDA profile of the steel without loading is shown in Fig. 2.4. The applied stress is 0.5 of the ultimate tensile strength, and the higher temperature peak reaches saturation faster than the lower temperature peak, implying that the occupancy proceeds faster in sites of higher  $E_b$ .

The occupancy of trap sites proceeds through trapping and detrapping processes of hydrogen as a function of trapping parameters,  $k$  and  $p$ , in the McNabb-Foster diffusion equation. Kasuya and Fuji numerically solved Eqs. (2.21) and (2.22) for two classes of traps [26]. The traps were characterized by the magnitude of  $N_t k_i / p_i$  of 20 and 3 respectively for the first and second class of traps, i.e., deeper trapping in the first class. Calculations were conducted for the entry of hydrogen from one side of a plate specimen, and the calculated distributions along the thickness of the plate before the steady state was attained showed that the occupancy of the deeper trap sites proceeded slower in the middle part of the specimen. The result is in contrast with Fig. 2.11 and Eq. (2.30) for the equilibrium partition. Effects of trapping parameters and/or initial conditions on kinetics of partition are subjects to be examined.

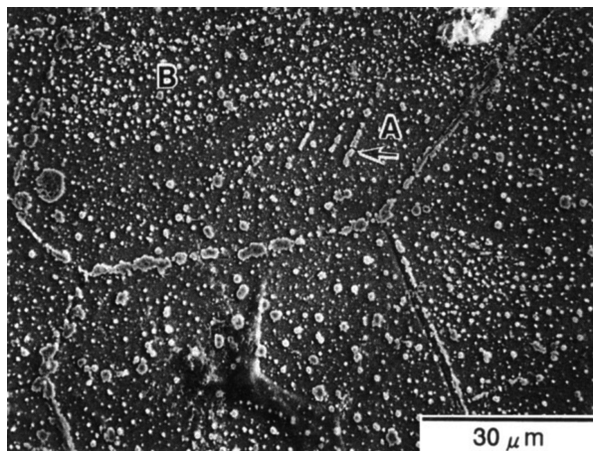
## 2.3 Visualization of Hydrogen Distribution

Effects of microstructures on embrittlement are to be examined firstly with respect to interactions of hydrogen with microstructural elements. However, experimental information on hydrogen effects is mostly averaged over the whole or a bulky portion of specimen. The observation of the location of hydrogen is then useful for distinguishing the role of microstructural elements in embrittlement.

Tritium is a radioactive isotope of hydrogen, and tritium autoradiography is a well-established technique for visualizing hydrogen distributions [27, 28]. Tritium autoradiography exhibits the distribution of Ag particles in a nuclear emulsion layer decomposed of AgBr by the 18.6 keV  $\beta$ -ray emitted from tritium. The emulsion film is deposited normally over a very thin intermediate collodion layer on the surface of tritiated specimen. Microstructures of the metal corresponding to the distribution of Ag particles can be revealed simultaneously when the metal surface has been prepared for metallographic observation. The penetration depth of the  $\beta$ -ray is about 1  $\mu\text{m}$  in iron-base alloys [28], and the spatial resolution of autoradiography is limited by the size of AgBr particles. Before coating the emulsion film, the tritiated specimens are normally exposed at room temperature so as to diffuse out extraneous tritium for the safety on manipulation. In this case, observed Ag particles exhibit strongly trapped sites for non-diffusive tritium.

Figure 2.12 [29] shows a tritium autoradiograph of a low-carbon ferritic steel specimen strained by 5 % at 193 K. Besides accumulation along grain boundaries, the arrows A and B in Fig. 2.12 indicate a columnar distribution and a band-like assembly, respectively, while the distribution within a grain is fairly uniform when

**Fig. 2.12** Tritium autoradiograph of a ferritic steel tensile strained by 5 % at  $-80\text{ }^{\circ}\text{C}$  (Aoki et al. [29])



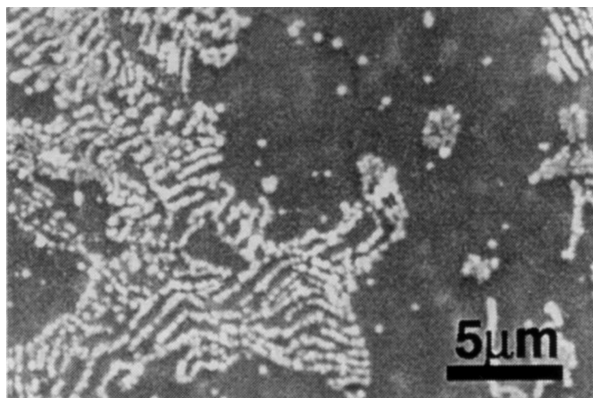
deformed at room temperature. The distributions exhibit strongly trapped sites of tritium, and the sites correspond well to slip bands that appeared on the surface of specimens.

Alternatively, a digital image technique using imaging plate (IP) in terms of tritium radioluminography has been developed [30]. The IP technique utilizes photostimulated luminescence and has a high sensitivity with a large dynamic range of about five orders. The IP enables to obtain not only two-dimensional distributions but also the concentrations of tritium. However, the IP needs a long exposure time of more than several tens hours, and the spatial resolution is limited by the size of pixels, currently a few tens  $\mu\text{m}$ .

Decomposition of AgBr in nuclear emulsion takes place also by chemical reactions with hydrogen. Hydrogen microprint technique (HMT) is a method to reduce AgBr in the nuclear emulsion coated on the surface by hydrogen diffusing out from the specimen [31]. Microscopic observation of Ag particles after fixing to remove unreacted AgBr reveals the distribution of emission sites of hydrogen on the surface. Since the development process is not necessary in HMT, the spatial resolution of Ag particles is generally better than tritium autoradiography. A substantial improvement of HMT has been devised, and 0.1  $\mu\text{m}$  in the spatial resolution of Ag particles and 40 % in the detection efficiency of hydrogen have been reported [32]. Figure 2.13 [32] is a SEM micrograph of HMT of a ferrite-pearlite steel plate specimen of 1.8 mm in thickness to which hydrogen was introduced from the opposite side. Preferential evolution of hydrogen from the interface of cementite in pearlite phase is clearly revealed.

Similarly, the silver decoration technique utilizes reduction of  $\text{Ag}^+$  ion in a solution by hydrogen. The specimen is immersed in a solution containing  $\text{AgNO}_3$  and a small amount of KCN and then is rinsed with water and dried. Adsorbed atomic hydrogen on the metal surface is thought to reduce  $\text{Ag}^+$  to Ag. Experiments with hydrogen-charged nickel specimens demonstrated different densities of Ag

**Fig. 2.13** Scanning electron micrograph of hydrogen microprint using gelatin-hardening for a ferrite-pearlite steel (Ichitani et al. [32]. Reprinted with permission from The Iron & Steel Inst. Japan)



particles between neighboring grains or in annealing twins [33]. High densities along slip lines and at grain boundary junctions were also revealed [33].

It should be noticed that states of detected hydrogen in specimen are not always the same between HMT and tritium autoradiography, diffusive in the former while normally non-diffusive in the latter. Observed distributions of Ag particles by HMT indicate desorption sites of hydrogen diffusing out from the surface while autoradiography shows stably trapped sites of hydrogen. Accordingly, the two methods are complementary to each other and the use of the two together is useful for examining interactions of microstructures with hydrogen.

Scanning secondary ion mass spectroscopy (SIMS) is a high sensitivity tool for detecting hydrogen of concentrations as low as the order of ppb. Sputtering the surface of the specimen with a focused primary ion beam ejects secondary ions and exhibits the distribution of elements [34]. The mass/charge ratio of secondary ions is measured with a mass spectrometer. The SIMS method is useful to detect the distribution of hydrogen interacting with different elements. Figure 2.14 [25] shows distributions of  $D^-$ ,  $Si^-$  and  $P^-$  in a cold-drawn eutectoid steel specimen subjected to a delayed fracture test in a corrosive solution containing deuterium. Accumulation of deuterium in segregation zones of Si and P is evident. Repeated sputtering of the same area by the primary ion in SIMS measurement gives a three-dimensional distribution image, and the vacuum environment for SIMS enables to distinguish diffusive and non-diffusive types of trapping in the specimen.

Response of hydrogen to external excitations is generally very weak, but neutron interacts strongly with proton. Neutron tomography (NT) is a technique to produce three-dimensional images of the absorbance of neutrons in materials. Hydrogen distributions around blisters formed in iron by electrochemically introduced hydrogen were detected using NT with a spatial resolution of about 25  $\mu m$  [35]. Hydrogen-charging produced cracks and blisters, and a hydrogen-enriched zone of 50  $\mu m$  wide was detected surrounding cracks. Hydrogen also accumulated at the sample surface having the highest concentration at blistered areas. The hydrogen accumulation around the cracks could be removed like diffusive hydrogen by a mild temperature treatment.

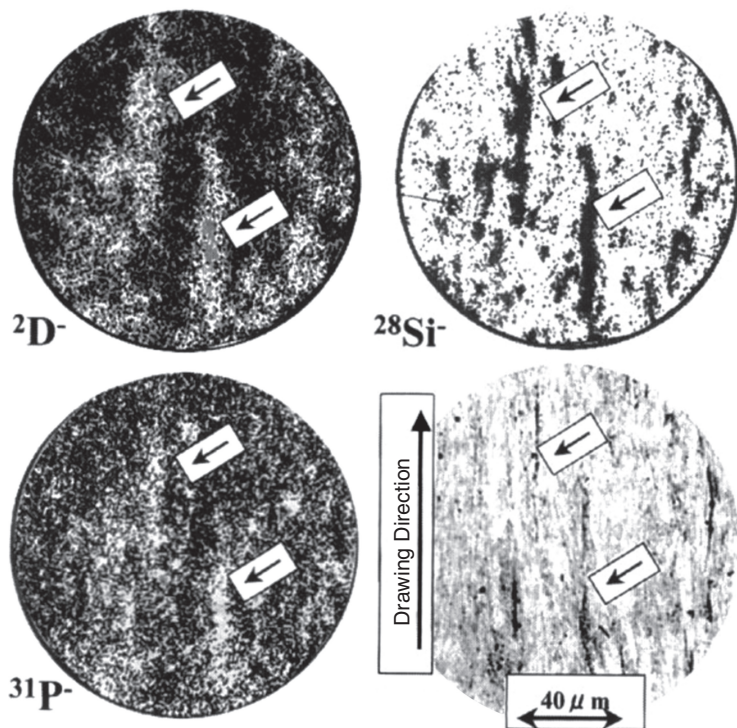


**Fig. 2.14** Scanning secondary ion mass spectrometry images of cold-drawn eutectoid steel specimens dipped in a 20 %  $\text{NH}_4\text{SCN}$  deuterium-added aqueous solution. The lower right micrograph shows microstructures (Takai et al. [25]. Reprinted with permission from The Iron & Steel Inst. Japan)

## References

1. J.R.G. da Silva, S.W. Stafford, R.B. McLellan, *J. Less Common Met.* **49**, 407–420 (1976)
2. O.D. Gonzalez, *Trans. Metall. Soc. AIME* **245**, 607–612 (1969)
3. A.J. Kurnick, H.H. Johnson, *Metall. Trans. A* **6A**, 1087–1091 (1975)
4. K. Yamakawa, T. Tsuruta, S. Yoshizawa, *Boshoku-Gijutsu* **30**, 443–449 (1981)
5. R.A. Oriani, P.H. Josephic, *Acta Metall.* **27**, 997–1005 (1979)
6. K. Yamakawa, in *Advances in Delayed Fracture Solution* (Iron and Steel Institute of Japan, Tokyo, 1997), pp. 77–81
7. P.A. Redhead, *Vacuum* **12**, 203–211 (1963)
8. W.Y. Choo, J.Y. Lee, *Metall. Trans. A* **13A**, 135–140 (1982)
9. J.L. Lee, J.Y. Lee, *Metall. Trans. A* **16A**, 468–471 (1985)
10. K. Ono, M. Meshii, *Acta Metall.* **40**, 1357–1364 (1992)
11. K. Takai, G. Yamauchi, M. Nakamura, M. Nagumo, *J. Jpn. Inst. Metals* **62**, 267–275 (1998)
12. H.E. Kissinger, *Anal. Chem.* **29**, 1702–1706 (1957)
13. J.Y. Lee, J.L. Lee, *Philos. Mag. A* **56**, 293–309 (1987)
14. R.A. Oriani, *Acta Metall.* **18**, 147–157 (1970)
15. K. Takai, R. Watanuki, *ISIJ Int.* **43**, 520–526 (2003)



16. A. Turnbull, R.B. Hutchings, D.H. Ferriss, *Mater. Sci. Eng.* **A238**, 317–328 (1997)
17. T. Yamaguchi, M. Nagumo, *ISIJ Int.* **43**, 514–519 (2003)
18. A. McNabb, P.K. Foster, *Trans. Metall. Soc. AIME* **227**, 618–627 (1963)
19. M. Enomoto, D. Hirakami, T. Tarui, *ISIJ Int.* **46**, 1381–1387 (2006)
20. Y. Sato, K. Fujita, H. Suzuki, K. Takai, Y. Hagiwara, K. Maejima, N. Miyabayashi, *CAMP ISIJ* **21**, 1375 (2008)
21. B.G. Pound, G.A. Wright, R.M. Sharp, *Acta Metall.* **35**, 263–270 (1987)
22. J.P. Hirth, B. Carnahan, *Acta Metall.* **26**, 1795–1803 (1978)
23. R.B. McLellan, *Acta Metall.* **27**, 1655–1663 (1979)
24. D.N. Beshers, *Acta Metall.* **6**, 521–523 (1958)
25. K. Takai, J. Seki, Y. Homma, *Tetsu-to-Hagané* **81**, 1025–1030 (1995)
26. T. Kasuya, M. Fuji, *J. Appl. Phys.* **83**, 3039–3048 (1998)
27. P. Lacombe, M. Auouturier, J. Chéne, in *Hydrogen Embrittlement and Stress Corrosion Cracking*, ed. by R. Gibara, R.F. Hehemann (ASM, Metals Park, 1984), pp. 79–102
28. J. Chéne, A.M. Brass, in *Hydrogen Effects in Materials*, ed. by A.W. Thompson, N.R. Moody (TMS, Warrendale, 1996), pp. 47–59
29. M. Aoki, H. Saito, N. Mori, Y. Ishida, M. Nagumo, *J. Jpn. Inst. Metals* **58**, 1141–1148 (1994)
30. H. Saitoh, T. Hishi, T. Misawa, T. Ohnishi, Y. Noya, T. Matsuzaki, T. Watanabe, *J. Nucl. Mater.* **258/263**, 1404–1408 (1998)
31. J. Overjero-Garcia, *J. Mater. Sci.* **20**, 2623–2629 (1985)
32. K. Ichitani, M. Kanno, S. Kuramoto, *ISIJ Int.* **43**, 496–504 (2003)
33. T. Shober, C. Dieker, *Metall. Trans. A* **14A**, 2440–2442 (1983)
34. K. Takai, J. Seki, Y. Homma, *Mater. Trans. JIM* **36**, 1134–1139 (1995)
35. A. Griesche, E. Dabah, T. Kannengiesser, N. Kardjilov, A. Hilger, I. Manke, *Acta Mater.* **78**, 14–22 (2014)





<http://www.springer.com/978-981-10-0160-4>

Fundamentals of Hydrogen Embrittlement

Nagumo, M.

2016, IX, 239 p. 140 illus., 131 illus. in color., Hardcover

ISBN: 978-981-10-0160-4